# Asymmetric droplet splashing

Jiguang Hao [1,*] Jie Lu,[1] Zihao Zhang,[1] Zhihu Wu,[1] Gengkai Hu,[1] and J. M. Floryan[2]
[1] *School of Aerospace Engineering, Beijing Institute of Technology, Beijing 100081, China*
[2] *Department of Mechanical and Materials Engineering, Western University, London, Ontario N6A 5B9, Canada*

(Received 20 August 2019; revised 29 December 2019; accepted 25 June 2020; published 21 July 2020)

The ideal droplet impact, i.e., the orthogonal impact on a smooth surface, results in the formation of an axisymmetric lamella followed by various symmetry-breaking instabilities. Impacts found in nature are nonideal, i.e., are affected by symmetry-breaking factors, e.g., surface topography, surface elasticity, impact nonorthogonality, etc. This work is focused on oblique impacts. The lamella retains a nearly circular shape during the early stages of such impacts, showing a weak effect of the inclination angle. A strong effect is observed during splashing which occurs at different locations along the lamella edge. The variations of the location of the border between the splash and no-splash zones as a function of the relevant parameters were determined. New features of the splashing referred to as abnormal splashing were observed at reduced ambient pressures. It is shown that the abnormal splashing is a direct consequence of the nonmonotonic variations of the threshold pressure as a function of the Weber number for orthogonal impacts. A simple model being able to capture the basic features of the splash process was proposed and validated through comparisons with the experimental results.

DOI: 10.1103/PhysRevFluids.5.073603

## I. INTRODUCTION

Following its impact on a dry, smooth surface, a droplet forms a thin radial lamella. The lamella detaches from the surface and ejects secondary droplets if the impact velocity exceeds a certain threshold, resulting in the splashing phenomenon. Droplet splashing is ubiquitous both in nature and in a variety of applications including aerosol formation, ink printing, spray coating, cooling, cleaning, combustion, and pesticide delivery. It has been studied by numerous researchers [1–4] following Worthington's original investigation [5]. Several mechanisms explaining splashing have been proposed, including the inertial dynamics [6–8], the air film dynamics under the lamella [9–16], and the lamella aerodynamics [17–19]. A consensus explaining the observed phenomena has yet to be reached [1], and this is due to the rapid droplet evolution and numerous contributing effects, including droplet properties (kinematics [6–8], surface tension [10,20–22], viscosity [20,23]), impact surface properties (wettability [24–26], roughness [6,7,9,20,22,27–30], moving velocity [31–34], inclination angle [10,35–38], temperature [39,40], and surface flexibility [41]), and ambient gas properties (pressure [23,28,29,32,38,42] and molecular weights [42]).

While most impacts encountered in nature and in applications are oblique, they have attracted limited interest [10,35–38] and remain rather poorly understood. Very recently, we investigated the suppression of droplet splashing on an inclined surface and developed a model to predict threshold parameters for upward and downward splashes [38]. The observation method (side view) provided

*hjgizq@bit.edu.cn

 

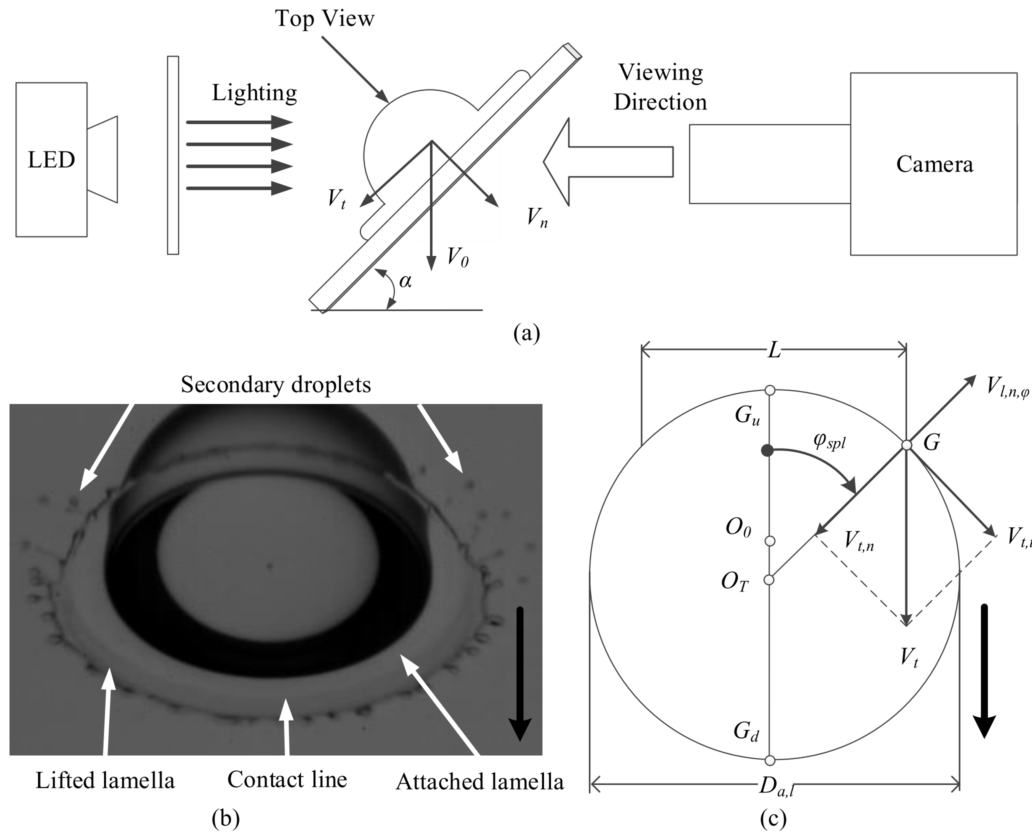


FIG. 1. (a) Sketch of the experimental setup. $V_n$ and $V_t$ stand for the normal- and tangential-to-the-surface components of $V_0$, respectively. (b) A typical image ($\alpha = 40^\circ$, We $= 513$). (c) Sketch of the top view of the evolution of lamella following droplet impact. $O_0$ and $O_T$ identify the initial impact point and the center of lamella at time $T$, respectively. $G_u$, $G$, and $G_d$ identify points at the lamella tip corresponding to the radial angles of $0^\circ$, $\varphi_{\rm spl}$, $180^\circ$, where $\varphi_{\rm spl}$ stands for the splash angle with splash occurring for $180^\circ > \varphi > \varphi_{\rm spl}$. $V_{l,n,\varphi}$ is the normal velocity component of the lamella tip at $G$. $V_{t,n}$ and $V_{t,t}$ stand for the normal- and tangential-to-the-lamella-edge velocity components of $V_t$, respectively. $L$ is the distance between the roots of the first-ejected secondary droplets on both sides of the lamella at the instant they are ejected. $D_{a,l}$ is the diameter of the attached lamella at the same instant. Black arrows point in the downward direction.

the means for observing droplet evolution along the vertical cut through the droplet, leaving the full three-dimensional structure unexplored. In order to observe the three-dimensional structure, we developed a new technique based on observation from underneath the impact surface. This method was originally used to observe the air film trapped underneath a droplet [15,43–50]. By decreasing the spatial resolution and by using droplet as a lens [49,50] [see Fig. 1(a)], we are able to increase the observation area and can identify several features of the impact process, including formation of the lamella, and its lifting and breakup into secondary droplets [see Figs. 1(b) and 4].

Four types of impacts were observed in this study: impacts with no splashing, with normal splashing, with upward-only splashing, and with wing splashing. The lamella remains attached to the surface for the no-splash impact. For the normal-splash impact, the splash occurs for the lamella segment $\varphi_{\rm spl} \leqslant \varphi \leqslant 180^\circ$ (see Fig. 4). Here the splash angle $\varphi_{\rm spl}$ is defined as the radial angle $\varphi$ measured downward from the slope line up to the location where splashing begins to occur [see Fig. 1(c)]. For the upward-only-splash impact, the splash occurs at the upward segment of the lamella for $0^\circ \leqslant \varphi \leqslant \varphi_{\mathrm{spl},d}$ [see Figs. 6(c) and 6(d)]. For the wing-splash impact, the splash occurs in the lamella segments $\varphi_{\mathrm{spl},u} \leqslant \varphi \leqslant \varphi_{\mathrm{spl},d}$ on both sides of the lamella [see Fig. 7(c)]. Here, $\varphi_{\mathrm{spl},u}$ and $\varphi_{\mathrm{spl},d}$ denote the radial angles marking the beginning and the end of the splash zone, respectively. Needless to say, $\varphi_{\mathrm{spl},u} = \varphi_{\mathrm{spl},d} = 180^\circ$ for a no-splash impact, $\varphi_{\mathrm{spl},u} = \varphi_{\mathrm{spl}}$, and $\varphi_{\mathrm{spl},d} = 180^\circ$ for the normal-splash impact. The upward-only and the wing splash are referred to as the abnormal splashes. Both the normal and the abnormal splashes display the up/down asymmetry.

We found that the lamella maintains an approximately circular shape during the early stages of the impact. We determined variations of the radial splash angle $\varphi_{\mathrm{spl}}$ as a function of the inclination angle $\alpha$, the Weber number $\mathrm{We} = \rho D_0 V_0^2/\sigma$, and the ambient pressure $P$, and observed abnormal splashing at reduced pressure. Here $\rho$ is the liquid density, $D_0$ the droplet diameter, $V_0$ the impact velocity, and $\sigma$ the surface tension. We extended the existing two-dimensional model predicting lamella tip velocity to three-dimensional configurations and used it to predict the lamella tip velocity around the spreading circle. The model predictions agree reasonably well with the experimental observations.

## II. EXPERIMENTAL SETUP

The experimental setup is shown in Fig. 1(a). By placing an LED light source (Godox SL-200W) about 50 mm away from the impact point, the droplet can be used as a lens to observe the impact process from underneath of the impact surface. A Photron SA1.1 high-speed camera was used to record the impact process at rates of up to 40 000 fps and with a spatial resolution of up to 10 $\mu$m/pixel. To achieve the required spatial resolution, a 105 mm microlens (Nikon AF Micro Nikkor 1:2.8D) and three spacer rings (Nikon) were used. The resolution of the images is up to 512 $\times$ 512. A typical image recorded using this method displayed in Fig. 1(b) shows rich phenomena including formation of lamella, its lifting, propagation of contact line separating lifted and attached segments of lamella, and formation of secondary droplets. As shown in Fig. 1(b), the area where lamella is attached to the surface is brighter than the area where lamella is detached from the surface, and this is due to different refraction of light. The boundary between these two areas is referred to as the contact line.

The spreading diameter is determined by extracting the location of the contact line using the software IMAGEJ. The error in identification of the location of contact line is less than one pixel for splashes with $\varphi_{\mathrm{spl}} > 90^\circ$, which results in error in measuring diameter of no more than two pixels [see Fig. 5(b)]. This error increases for splashes with $\varphi_{\mathrm{spl}} < 90^\circ$ up to six pixels as the contact line is more diffused in the images and uncertainty in the determination of its location is can be up to three pixels [see Figs. 1(b) and 5(a)]. As the typical diameters are larger than 150 pixels at the instant of the first ejection of the secondary droplets, the error of determination of lamella diameter is either less than 1.3%($\varphi_{\mathrm{spl}} > 90^\circ$) or less than 4.0%($\varphi_{\mathrm{spl}} > 90^\circ$).

Ethanol of density $\rho = 791\,\mathrm{kg/m^3}$, dynamic viscosity $\mu = 1.19\,\mathrm{mPa\,s}$, and surface tension $\sigma = 22.9\,\mathrm{mN\,m^{-1}}$ [22,32,38] was used in the experiments and the ambient temperature was kept at $24 \pm 1\,^\circ\mathrm{C}$ A syringe pump with a flat-tipped needle was used to create droplet which was released from height $H$ above the impact surface. The droplet release occurred naturally by slowly increasing its mass until its weigh overcome adhesion forces. This process resulted in droplets with diameter $D_0 = 1.74 \pm 0.05\,\mathrm{mm}$. As the droplet diameter is close to the capillary length [50] of ethanol, $l_c = \sqrt{\sigma/(\rho g)} = 1.72$ mm, no shape oscillations were observed before the impact. Here $g = 9.81\,\mathrm{m/s^2}$ is the gravitational acceleration. The impact velocity $V_0$ was varied from 1.5 to 3.24 m/s by changing release height $H$, with the corresponding Weber numbers varying from 135 to 643.

The impact surface was made from transparent acrylic with the mean roughness amplitude of $\mathrm{R}_a = 0.011\,\mu\mathrm{m}$ [22]. A rotary table with inclination angle $\alpha$ in the range of 0°–90° was used to adjust $\alpha$ with a precision of ±0.1° [38] [see Fig. 1(a)]. The experimental apparatus was placed in a transparent vacuum chamber where gas pressure $P$ could be adjusted in a range of 10–101 kPa.

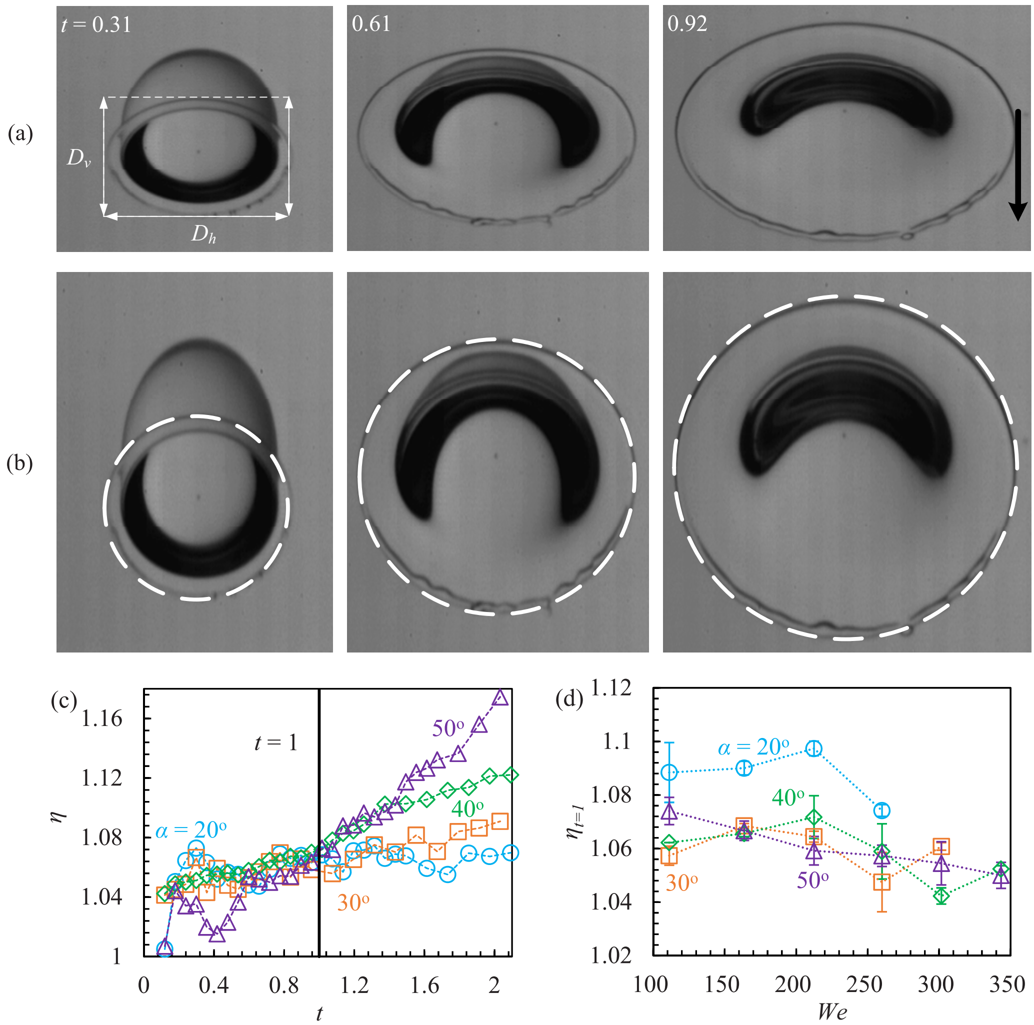


FIG. 2. (a) Images of the impacting droplet for $\alpha = 40^\circ$, We $= 361$. $D_v$ and $D_h$ are the vertical and horizontal spreading diameters (see Movie S1 for more details [51]). (b) The same images transformed to imitate viewing in the direction normal to the impacted plate with dashed circles illustrating lamella location. (c) Variations of the diameter ratio $\eta = D_{v\_a}/D_h$, where $D_{v\_a} = D_v/\sin\alpha$, as function of $t$ and $\alpha$ for We $= 260$. (d) Variations of $\eta$ at $t = 1$ as a function of We and $\alpha$. Error bars indicate the standard deviation.

## III. RESULTS AND DISCUSSION FOR ATMOSPHERIC PRESSURE

### A. Evolution of the lamella shape

Evolution of the lamella shape following an oblique impact is not well understood. Our observations show that the droplet moves along the surface due to the existence of $V_t$ [see Fig. 1(a)]. Consequently, one would expect a noncircular lamella. We begin the discussion of the spreading process for Weber numbers below the splash threshold where the boundaries between the three phases (gas, liquid, and solid) can be clearly identified.

As shown in Fig. 2(a), variations of the horizontal ($D_h$) and vertical ($D_v$) spreading diameters as functions of nondimensional time $t = TV_0/D_0$ can be determined using the recorded images, where $T$ is the time measured from the beginning of the impact. Images displayed in Fig. 2(b)

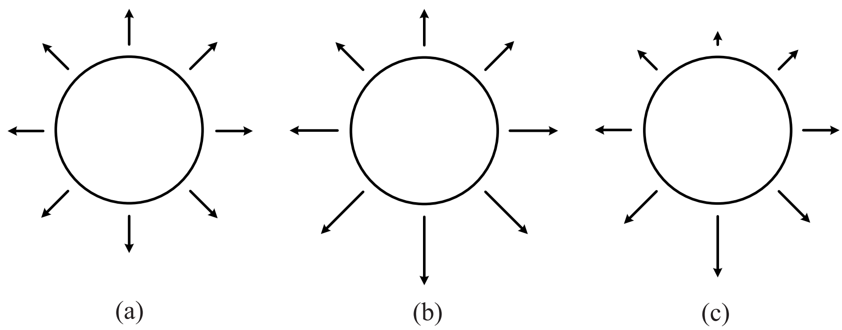

FIG. 3. Sketch of the outward velocity (solid arrows) along the periphery following impacts on surfaces with $\alpha = 0^\circ$ (a), $\alpha = b$ (b), and $\alpha = c$ (c), where $0^\circ < b < c$. Circles illustrate positions of the spreading lamella tip.

correspond to the viewing direction being orthogonal to the impacted plate, i.e., these are images taken from Fig. 2(a) transformed by stretching the vertical direction by a factor of $1/\sin(\alpha)$. The spreading lamella retains a nearly circular shape during the early stages of the impact, i.e., $D_h$ approximately equals $D_v/\sin(\alpha)$. This effect is documented through time variations of the diameter ratio $\eta = [D_v/\sin(\alpha)]/D_h$ displayed in Fig. 2(c), which demonstrates that $\eta < 1.1$ for time up to $t = 1$, but increases thereafter with a more rapid increase for larger $\alpha$'s. The first droplet ejection typically occurs before time reaches $t = 1$, with $\eta$ being at that instant less than 1.1 for all Weber numbers used in the experiment [see Fig. 2(d)]. The shape of the spreading lamella can therefore be assumed as being circular during the early stages of the impact process, which means that our results can be viewed as a leading order approximation with the error being $O(\epsilon)$ or smaller, where $\epsilon = |1 - \eta|$. This assumption is used in the formulation of the definition of the splash angle $\varphi_{\mathrm{spl}}$ [see Fig. 1(c)] and its determination [see Figs. 5(a) and 5(b)], as well as in building the theoretical model, where the outward velocity $V_{l,n,\varphi}$ of the lamella tip along the circular periphery is asymmetric on an inclined surface, as shown in Fig. 3; please see Sec. III C for detailed information.

### B. Progressive splash suppression

Figure 4 shows the time evolution of droplets impacting on surfaces with various inclination angles $\alpha$ at We = 416. Each row represents a different $\alpha$, each column represents a different $t$. The images demonstrate progressive splash suppression with an increase of $\alpha$ consistent with previous research [38]. Figure 4(a) illustrates the splash occurring all around the lamella. Figures 4(b) and 4(c) show elimination of splash in the upwards segments of the lamella with the length of the splashing portion decreasing with an increase of $\alpha$. Figure 4(d) demonstrates that no splash occurs when the inclination angle reaches 50°.

An increase of We leads to an increase of the splashing portion of the lamella as illustrated in Figs. 5(a) and 5(b). Based on the experimental observations that the lamella retains a nearly circular shape during the early stages of the impact process, the position of the border between the splashing and nonsplashing lamella segments corresponds to the radial angle $\varphi_{\mathrm{spl}} = \arcsin(L/D_{a,l})$ [see Fig. 1(c)] for definitions of $L$ and $D_{a,l}$). Figure 5(a) explains how these distances are measured. When the border between the splash and no-splash zones is located below the center of the attached lamella, $\varphi_{\mathrm{spl}} = 180^\circ - \arcsin(L/D_{a,l})$, as illustrated in Fig. 5(b).

Figure 5(c) shows variations of $\varphi_{\mathrm{spl}}$ as a function of We and $\alpha$. The data represent averages of data extracted from at least three experiments. The splashing portion of the lamella increases with an increase of We ($\varphi_{\mathrm{spl}}$ decreases). Increase of the inclination angle results in higher We's required to trigger splashing on the same portion of lamella.

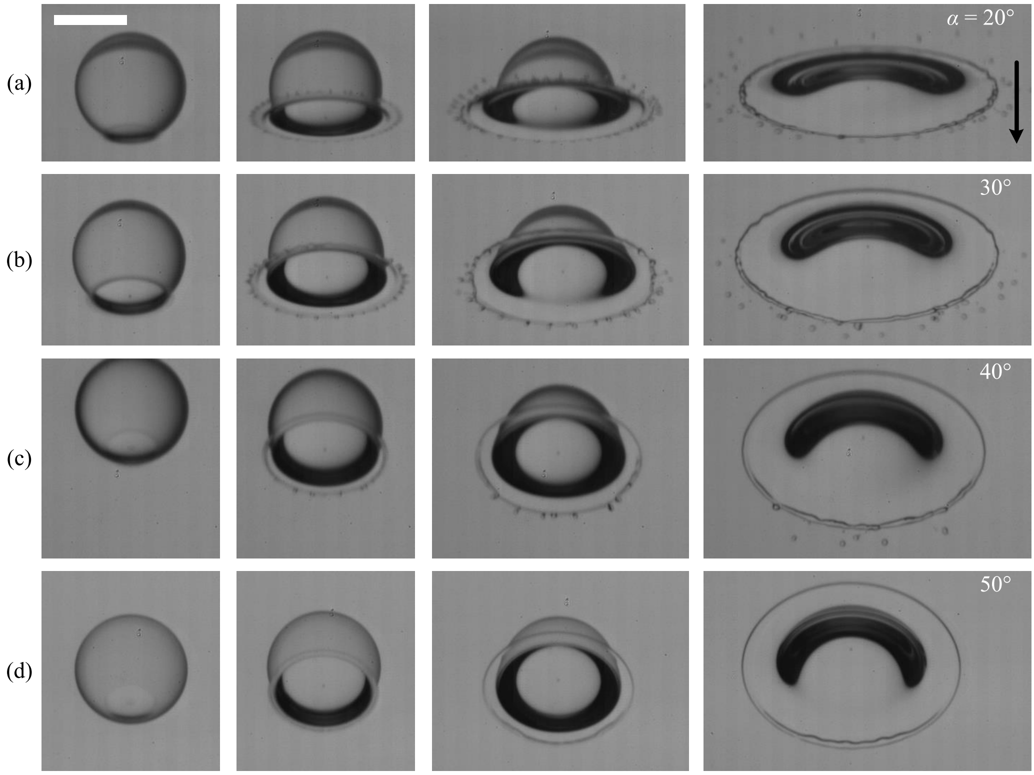


FIG. 4. Effect of the inclination angle $\alpha$ on the droplet splashing for We $= 416$ (see Movie S2 for more details [51]). The scale bar corresponds to 1.0 mm. (a) $\alpha = 20^\circ$, splash occurs everywhere around the lamella. (b) $\alpha = 30^\circ$ and (c) $\alpha = 40^\circ$, splash occurs only at a part of the lamella. (d) $\alpha = 50^\circ$, there is no splash.

### C. Discussion

To interpret the experimental results, the impact velocity $V_0$ is decomposed into the normal-to-the-surface ($V_n$) and parallel-to-the-surface ($V_t$) components [see Fig. 1(a)], i.e.,

$$V_n = V_0 \cos\alpha, \quad V_t = V_0 \sin\alpha. \tag{1}$$

$V_t$ can be further decomposed into the normal-to-the-lamella-tip ($V_{t,n}$) and tangential-to-the-lamella-edge ($V_{t,t}$) components [see point $G$ in Fig. 1(c)]

$$V_{t,n} = V_t \cos\varphi, \quad V_{t,t} = V_t \sin\varphi, \tag{2}$$

where $\varphi$ is the radial angle giving location of point $G$ and advantage was taken of experimental observations showing that the lamella retains a nearly circular shape during the early stages of the impact.

Since the splash is symmetric with respect to the slope, it is enough to analyze the lamella movement for $\varphi \in \langle 0^\circ, 180^\circ \rangle$. As proposed by Gordillo and Riboux [19], it is the gas lubrication layer underneath the lamella tip that dominates the vertical lift force which drives the splashing. The lubrication pressure is proportional to the normal-to-the-lamella-tip velocity component $V_{l,n,\varphi}$ which, therefore, needs to be determined in the analysis, whereas the tangential-to-the-lamella-tip velocity component $V_{l,t,\varphi} = V_{t,t}$ plays no role in the splash onset. $V_{l,n,\varphi}$ results from two effects: the first one is the orthogonal impact with velocity $V_n$ leading to the spreading velocity $V_l$, determined

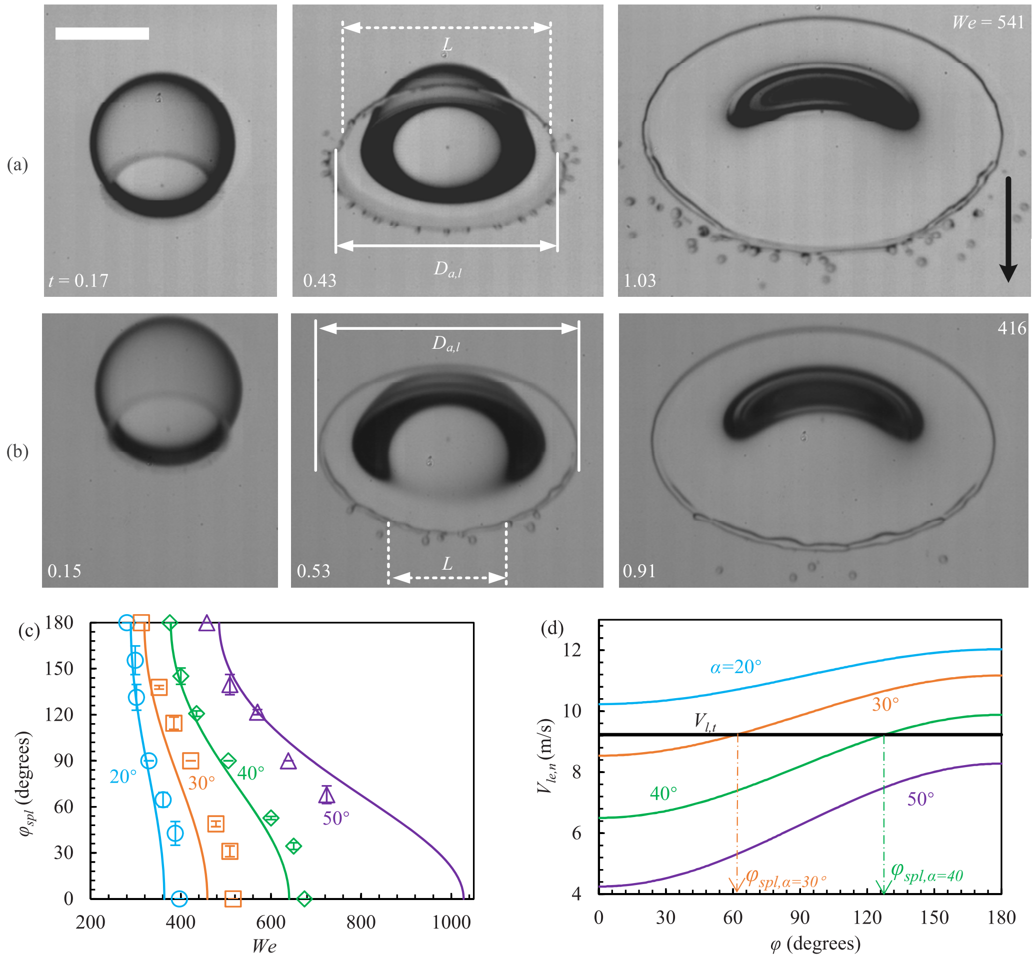


FIG. 5. (a) and (b) Droplet evolution during impact for $\alpha = 40^{\circ}$ and We $= 541$, 416, respectively (see Movie S3 for more details [51]). (c) Variations of the radial splash angle $\varphi_{\mathrm{spl}}$ as a function of We and $\alpha$. Error bars indicate the standard deviation. Threshold Weber number for $\varphi_{\mathrm{spl}} = 0^{\circ}$ was determined for the upward splash, while in the case of $\varphi_{\mathrm{spl}} = 180^{\circ}$ it was determined for the downward splashes, resulting in the absence of error bars. The upward splash was not observed for $\alpha = 50^{\circ}$ even at the highest We used in this study and, therefore, there are no data at $\varphi_{\mathrm{spl}} = 0^{\circ}$. Solid lines correspond to the theoretical results based on the modified RG model (see text for details). (d) Variations of the lamella tip velocity $V_l$ determined using the modified RG model for We $= 416$ as a function of $\varphi$. The black solid line represents the threshold velocity for the orthogonal impact.

using the relation proposed by Riboux and Gordillo (RG) [17],

$$V_l = \sqrt{3}/2\sqrt{D_0 V_n/2T} \tag{3}$$

the second effect is the tangential movement of the droplet with respect to the impact plate with velocity $V_t$. Combining these two effects gives a relation for $V_{l,n,\varphi}$ in the form

$$V_{l,n,\varphi} = V_l - V_{t,n} = V_l - V_0 \sin\alpha \cos\varphi \ (0^{\circ} \leqslant \varphi \leqslant 180^{\circ}). \tag{4}$$

This relation reduces for $\varphi = 0^{\circ}$,$180^{\circ}$ to relations giving the upward and downward velocities of the lamella tip presented in Ref. [38]. The outward velocity of the lamella tip at the beginning of droplet ejection ($V_{le,n,\varphi}$) is of special interest. This quantity can be determined by first computing the dimensionless lamella ejection time $t_e = 2T_eV_n/D_0$ from the momentum balance of the form [17]

$$\sqrt{3}/2\mathrm{Re}^{-1}t_e^{-1/2} + \mathrm{Re}^{-2}\mathrm{Oh}^{-2} = 1.21\, t_e^{3/2} \tag{5}$$

where $T_e$ stands for the moment of the initiation of lamella formation, $\mathrm{Re} = \rho V_n D_0/2\mu$ is the Reynolds number, and $\mathrm{Oh} = \mu/\sqrt{\rho D_0\sigma/2}$ is the Ohnesorge number, then determining $V_{le}$ using Eq. (3), and, finally, computing $V_{le,n,\varphi}$ using Eq. (4). Variations of $V_{le,n,\varphi}$ for $\mathrm{We} = 416$ determined in this manner as a function of $\varphi$ and $\alpha$ are illustrated in Fig. 5(d).

Splash occurs only if the velocity of the lamella tip exceeds a certain threshold $V_{l,t}$ [38]. This threshold is known for the orthogonal impact and can be used as a reference point for the oblique impact. The threshold Weber number for the orthogonal impact corresponds in our experiments to $\mathrm{We} = 286$, and this value combined with Eqs. (3) and (5) was used to determine $V_{l,t}$, which is marked in Fig. 4(d) using a thick black solid line. The lamella lifts up at locations along its circumference where $V_{le,n,\varphi} > V_{l,t}$. This means that it lifts up everywhere when $\alpha = 20^\circ$ [Fig. 4(a)]. Only a portion lifts up when $\alpha = 30^\circ$ [Fig. 4(b)] and $\alpha = 40^\circ$ [Fig. 4(c)]. The tip velocity is lower than $V_{l,t}$ everywhere when $\alpha = 50^\circ$ [Fig. 4(d)] and no splash occurs under such conditions.

For a Weber number resulting in a splash occurring at a certain $\alpha$, the lamella tip velocity $V_{le,n,\varphi}$ increases with $\varphi$ until $V_{le,n,\varphi} = V_{l,t}$, which marks the border between the splash and no-splash zones. This point corresponds in Fig. 5(d) to the intersection of the line showing variations of $V_{le,n,\varphi}$ as a function of $\varphi$ with the threshold $V_{l,t}$, and its position defines the threshold angle $\varphi_{\mathrm{spl},\alpha}$. These thresholds are marked in Fig. 5(d) in the case of $\alpha = 30^\circ$, $40^\circ$ as $\varphi_{\mathrm{spl},\alpha=30^\circ}$ and $\varphi_{\mathrm{spl},\alpha=40^\circ}$, respectively. Splash occurs for $\varphi > \varphi_{\mathrm{spl},\alpha}$ under otherwise identical conditions. The actual determination of the threshold angle starts with the substitution of the known $V_{le,n,\varphi}$ $(= V_{l,t})$ into Eqs. (3)–(5) and determination of the corresponding $\varphi_{\mathrm{spl}}$ for a specified We and $\alpha$. The predicted variations of $\varphi_{\mathrm{spl}}$ as a function of We and $\alpha$ displayed in Fig. 5(c) agree reasonably with the experimental data, which suggests that the splash onset is determined by the outward velocity of the lamella tip.

The simple model presented above does not consider many factors which could affect splashing, e.g., fluid movement inside the droplet, gravity effects, formation of various boundary layers, etc. While its predictions somewhat underestimate the experimental results for $\alpha = 20^\circ$–$40^\circ$ and overestimate a bit for $\alpha = 50^\circ$, they nevertheless properly capture the overall trends, which suggests that the model properly accounts for the dominant physical factors.

## IV. RESULTS AND DISCUSSION FOR THE REDUCED AMBIENT PRESSURE

### A. The constant Weber number case

Reduction of the ambient pressure $P$ in general suppresses droplet splashing in the sense that it occurs later while its pattern remains unchanged, i.e., the splashing occurs for $\varphi_{\mathrm{spl}} \leqslant \varphi \leqslant 180^\circ$. This is documented in Figs. 6(a), 6(b), 6(e), 7(a), 7(b), 7(d), and 8, and it is consistent with the previously reported observations [38,42]. There is, however, a narrow range of pressures where either the upward-only splashing, as illustrated in Figs. 6(c) and 6(d), or the wing splashing, as illustrated in Fig. 7(c), occurs. In Figs. 6(c) and 6(d) ejection from the downward portion of the lamella is observed after a fairly long time from the beginning of the impact. We define the upward-only splash based on the very initial stages of the impact and, accordingly, we classify these impacts of as upward only. The splash displayed in Fig. 7(c) is characterized by formation of droplet trains in the form of wings and we refer to it as the wing splash. The abnormal splashes were observed only at low inclination angles, i.e., they were observed for $\alpha = 20^\circ$ and $\alpha = 30^\circ$, but when the inclination angle increased to $\alpha = 40^\circ$, $\varphi_{\mathrm{spl}}$ increased monotonically with pressure reduction (see Fig. 8).

Results displayed in Fig. 6 demonstrate that splashing on a surface with $\alpha = 20^\circ$ is marginally affected by the ambient pressure if this pressure is larger than 51 kPa. For ambient pressures in the

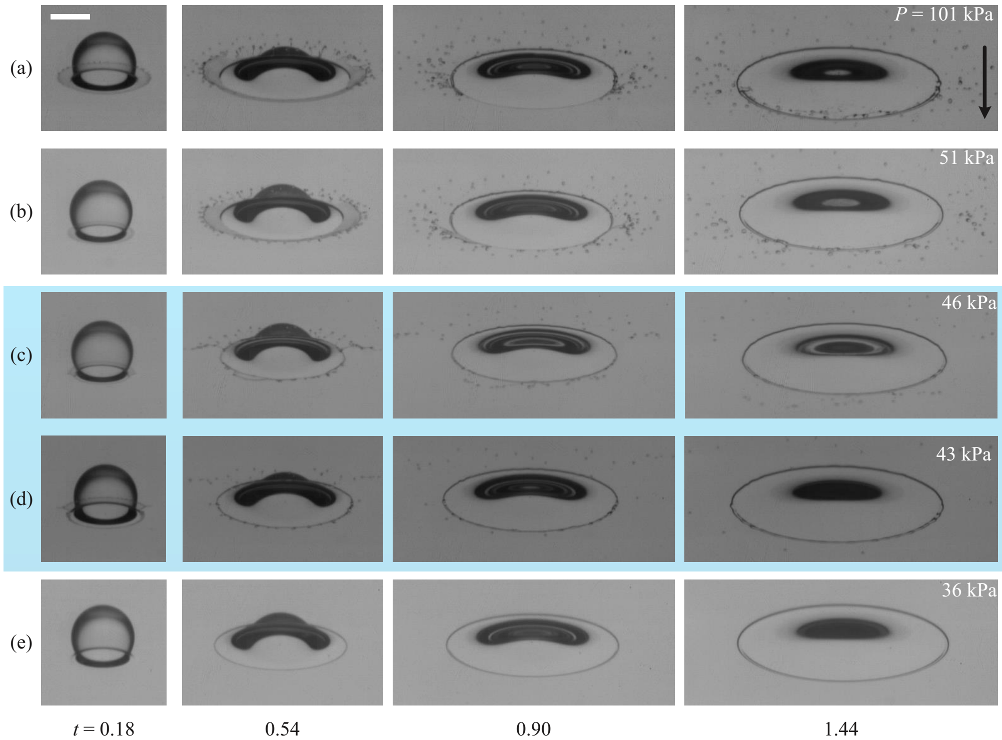


FIG. 6. Effect of the ambient pressure on the droplet splashing for $\alpha = 20^\circ$, We $= 593$ (see Movie S4 for more details [51]). Each column represents a different dimensionless time $t$ and each row represents a different ambient pressure. (a) $P = 101$ kPa, $\varphi_{\text{spl}} = 0^\circ$. (b) $P = 51$ kPa, $\varphi_{\text{spl}} = 0^\circ$. (c) $P = 42$ kPa, upward-only splashing. (d) $P = 39$ kPa, upward-only splashing. (e) $P = 36$ kPa, no splashing.

range $51 > P > 38.5$ kPa, the upward-only splashes occur. Decrease of the ambient pressure below 36 kPa eliminates splashing. Results displayed in Fig. 8 show no abnormal splashing for $\alpha = 40^\circ$ in the range of pressures used in this study.

Variations of $\varphi_{\text{spl}}$ as a function of $P$ were measured experimentally for We $= 593$. The blue ($51 > P > 38.5$ kPa) and orange ($36 > P > 31$ kPa) zones in Fig. 9(a) show that the widths of the zones for the abnormal splashing decrease with an increase of $\alpha$ until such splashes are eliminated, which occurs at $\alpha = 40^\circ$ for the conditions used in the experiments. The threshold pressure required to suppress the downward splash decreases with a decrease of the inclination angle in agreement with the previous study [38], as illustrated by points located furthest to the left in Fig. 9(a).

Variations of $\varphi_{\text{spl}}$ at a reduced pressure as a function of $\alpha$ and We can be predicted using information from the orthogonal impact [38]. As a starting point, the threshold pressure $P_t$ for such impact was measured for We in the range 286 to 643 with the results displayed in Fig. 9(b). The threshold pressure initially decreases, then increases, and then remains nearly constant as We increases, in agreement with the previous observations [38,42] at lower We's. These observations predicted another decrease with a further increase of We but such conditions could not be reproduced in our apparatus due to a limited height of its vacuum chamber. The reasons for the nonmonotonic variations are not understood [38,42] with their resolution deserving further attention.

Following the previous study [38], we assume that the threshold lamella tip velocities are the same for orthogonal and oblique impacts at the same pressure. Conditions leading to the same lamella tip velocities in both types of impacts need to be determined. As conditions vary along the lamella circumference in the oblique impact, this equivalence can be established only locally

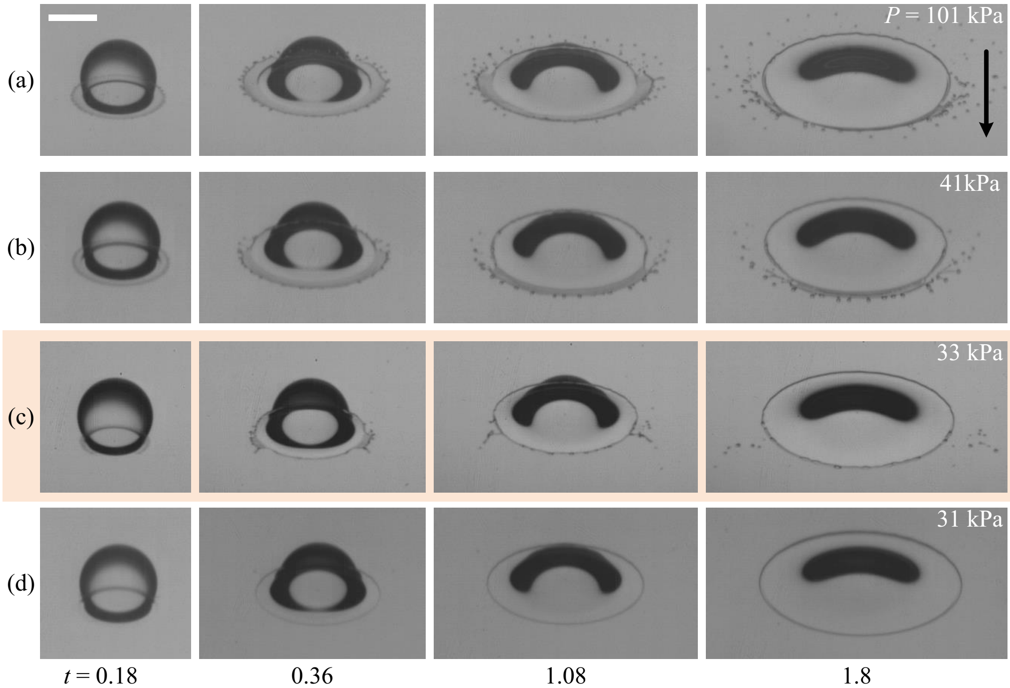


FIG. 7. Effect of the ambient pressure on droplet splashing for $\alpha = 30^\circ$, We = 593 (see Movie S5 for more details [51]). Rows and columns correspond to different $P$'s and times $t$, respectively. (a) $P = 101$ kPa, $\varphi_{\mathrm{spl}} = 0^\circ$. (b) $P = 41$ kPa, $\varphi_{\mathrm{spl}} = 84^\circ$. (c) $P = 33$ kPa. Wing splashing occurs for $71^\circ \leqslant \varphi \leqslant 127^\circ$. (d) $P = 31$ kPa, $\varphi_{\mathrm{spl}} = 180^\circ$.

leading to the concept of the local equivalent orthogonal impact velocity (EOIV). Figure 10 shows that EOIV is the orthogonal impact velocity which results in the lamella tip velocity $V_{le}$ equal to the lamella tip velocity $V_{le,n,\varphi}$ at location $\varphi$ (point $G$) during oblique impact with velocity $V_0$ and inclination angle $\alpha$. $V_{le,n,\varphi}$ can be determined using Eqs (3)–(5). We determine EOIV from Eqs. (3) and (5) using condition $V_{le} = V_{le,n,\varphi}$. Determination of the local equivalent orthogonal Weber number (EOWN) follows with $V_0$ being replaced by EOIV.

In the next step to predict $\varphi_{\mathrm{spl}}$, the local EOWN was determined for We and the position along the lamella circumference defined by $\varphi$ using Eqs (3)–(5). The results are illustrated in Fig. 9(b) for We = 593 using solid color lines. In the third and final step, $P_t$ is determined for $\varphi$ of interest by selecting this $\varphi$ on the right axis in Fig. 9(b), then determining EOWN for the inclination angle of interest and, finally, determining $P_t$ using data from the orthogonal impact. The relevant information flow is illustrated in Fig. 9(b) using the dash-dotted lines. The solid lines displayed in Fig. 11 were determined using the above process. Use of information presented in Fig. 11(a) permits theoretical determination of $\varphi_{\mathrm{spl}}$'s for various $P$'s (these $P$'s must be larger than $P$'s producing abnormal splashing) at We = 593 with the results being consistent with the experiments [see solid lines in Fig. 9(a)].

Figure 11(a) illustrates variations of the threshold pressure determined using the available theory and $P_t$ for the orthogonal impact as a function of $\varphi$ and $\alpha$ for We = 593. When $\alpha = 40^\circ$, $P_t$ decreases monotonically as $\varphi$ increases, which is consistent with the experimental results displayed in Fig. 8. When $\alpha = 30^\circ$, $P_t$ initially decreases and then increases with $\varphi$ which characterizes the wing splashing displayed in Fig. 7(c). When $\alpha = 20^\circ$, $P_t$ remains constant for $\varphi <\sim 45^\circ$ and $\varphi >\sim 105^\circ$ but increases with $\varphi$ for $45^\circ < \varphi < 105^\circ$ which characterizes the upward-only splashing

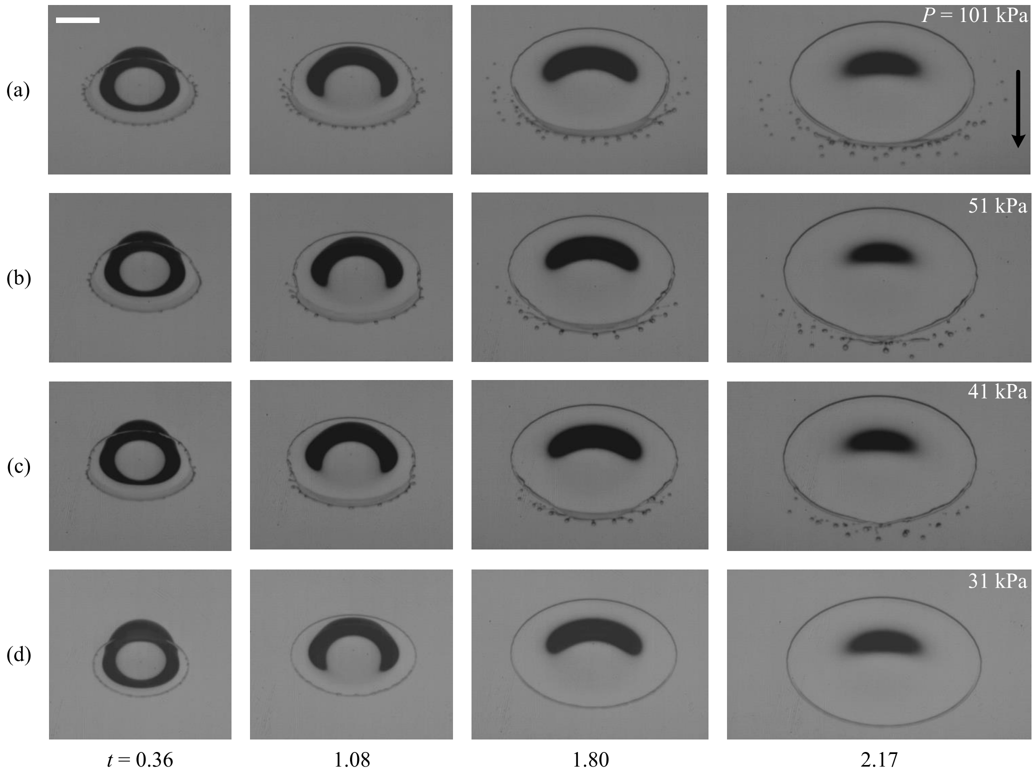


FIG. 8. Effect of the ambient pressure on the droplet splashing for $\alpha = 40^\circ$, We = 593 (see Movie S6 for more details [51]). Each column represents a different dimensionless time $t$ and each row represents a different ambient pressure. (a) $P = 101$ kPa, $\varphi_{\text{spl}} = 64^\circ$. (b) $P = 51$ kPa, $\varphi_{\text{spl}} = 108^\circ$. (c) $P = 41$ kPa, $\varphi_{\text{spl}} = 117^\circ$. (d) $P = 31$ kPa, $\varphi_{\text{spl}} = 180^\circ$.

documented in Figs. 6(c) and 6(d). The blue area in Fig. 11(a) indicates pressure range (36–46 kPa) resulting in the upward-only splashing for $\alpha = 20^\circ$ while the light-brown area indicates pressure range (36.0–42.8 kPa) for the wing splashing at $\alpha = 30^\circ$. The predicted ranges agree qualitatively with the results displayed in Fig. 9(a), where the pressure range for the abnormal splashing at $\alpha = 20^\circ$ is larger than that at $\alpha = 30^\circ$.

Information in Fig. 11(a) is also used to determine $\varphi_{\text{spl}}$'s for various pressures at a certain $\alpha$ and We = 593, with the green dash-dotted line illustrating the information flow required for the determination of this angle. To illustrate use of this figure, consider ambient pressure $P = 80$ kPa which is marked using black dotted line. This pressure is selected as it is higher than pressures leading to abnormal splashing; analysis of abnormal splashing is presented later in this discussion. If $P_t$ at a given $\varphi$ and $\alpha$ is higher than 80 kPa, the lamella does not splash at this location at this inclination angle and $P = 80$ kPa. Otherwise, splashing occurs. Intersection of line $P_t(\varphi)$ with the line giving the ambient pressure $P = 80$ kPa defines the threshold angle $\varphi_{\text{spl},\alpha}$ with splashing occurring for $\varphi > \varphi_{\text{spl},\alpha}$. This threshold is marked as $\varphi_{\text{spl},\alpha=40^\circ}$. The theoretically determined $\varphi_{\text{spl}}$'s are illustrated using solid lines in Fig. 9(a) and are consistent with the experimental data points given by symbols in Fig. 9(a).

Figure 11(b) provides a closer look at impacts with $\alpha = 20^\circ$, where ranges of threshold pressure leading to the normal splash ($P > 46$ kPa), the upward-only splash ($46 > P > 36$ kPa), and no splash ($P < 36$ kPa) can be identified for We = 593. The reader may recall that the normal splash for such $\alpha$ results in splashing for $\varphi_{\text{spl}} \leqslant \varphi \leqslant 180^\circ$ and upward-only splash gives splashing for

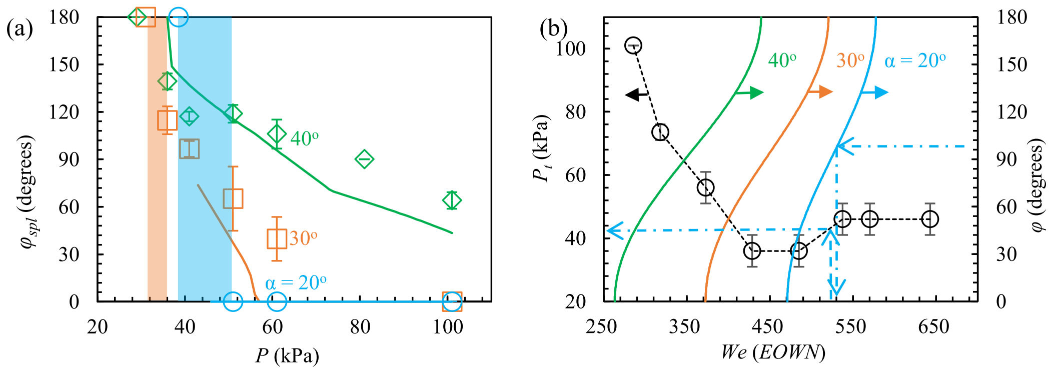


FIG. 9. (a) Variations of $\varphi_{\text{spl}}$ as a function of $P$ for We = 593. Error bars indicate the standard deviation. The blue and orange zones identify conditions leading to the abnormal splashing for $\alpha = 20^\circ$ and $\alpha = 30^\circ$, respectively. The solid lines illustrate theoretical results. (b) Variations of $P_t$ as a function of We for the orthogonal impact (black circles), where error bars indicate the uncertainty, and variations of the local EOWN (solid lines) as a function of the radial angle $\varphi$ for We = 593. Dash-dotted lines illustrate flow of information used in the theoretical determination of $P_t$ required to initiate splashing at a given $\varphi$.

$0^\circ \leqslant \varphi \leqslant \varphi_{\text{spl},d}$. To explain use of this plot in predicting splashing properties, select ambient pressure $P = 41$ kPa. Splashing occurs for the lamella segment $0^\circ < \varphi < \varphi_{\text{spl},d} =\sim 76^\circ$ as $P_t$'s required to produce splash for $\varphi >\sim 76^\circ$ are larger than this pressure. Images displayed in Fig. 7(d) show that splashing does indeed occur for $\varphi \leqslant 68^\circ$, which is in a reasonable agreement with these predictions. Increasing the ambient pressure to $P = 43$ kPa triggers splashing below $\varphi_{\text{spl},d} =\sim 87^\circ$, which compares favorably with images displayed in Figs. 6(c) and 6(d).

The wing splash displayed in Fig. 6(c) requires further discussion. The orange line in Fig. 11(c) illustrates variations of $P_t$ as a function of $\varphi$ for the conditions used in the experiment. The nonmonotonic character of these variations, which is similar to that reported for the orthogonal impact see Fig. 9(b), suggests that the same physical processes become important for both types of impacts under similar ambient pressures. The difference between oblique and orthogonal impacts is due to variations of the local conditions along the lamella circumference in the former case while these conditions remain constant in the latter case. Variation of the local conditions lead

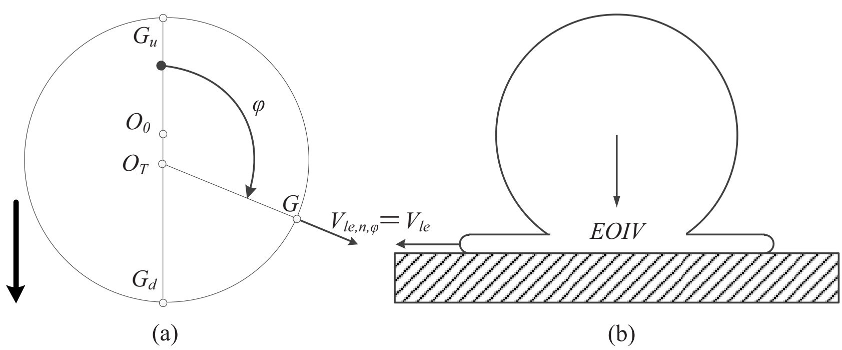


FIG. 10. Sketch explaining concept of the local equivalent erthogonal impact velocity (EOIV). (a) Top view of the oblique impact. Symbols are as indicated in Fig. 1(c). $V_{le,n,\varphi}$ is the lamella tip velocity at the moment of initiation of lamella formation at the specified location ($\varphi$) along the lamella, specified inclination angle ($\alpha$), and specified impact velocity ($V_0$). Black arrow points in the downward direction. (b) Side view of the orthogonal impact. $V_{le}$ is the lamella tip velocity at the moment of initiation of lamella formation with the impact velocity $V_0$ set to be equal to the EOIV.

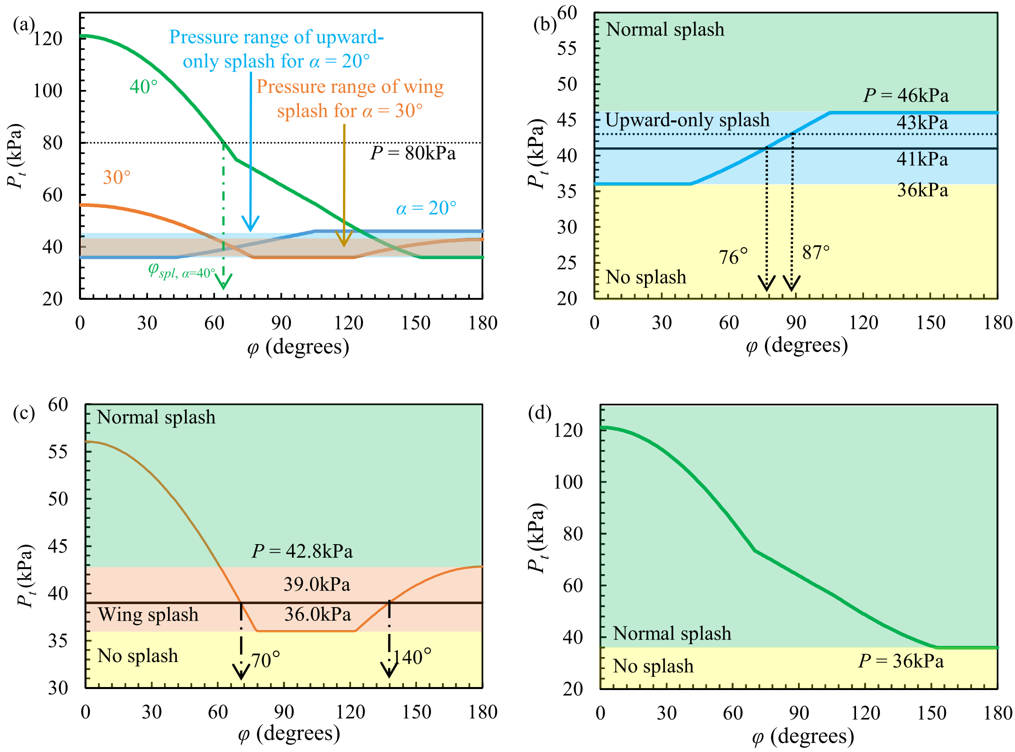


FIG. 11. (a) Variations of the theoretically determined threshold pressure as a function of the radial angle $\varphi$ for We $= 593$ and $\alpha = 20°$ (blue line), 30° (orange line), and 40° (green line). The green dash-dotted lines illustrate the information flow required for determination of $\varphi_{\text{spl}}$ from the known $P$. The blue and light-brown zones identify the pressure ranges for the abnormal splash for $\alpha = 20°, 30°$, respectively. (b) Variations of the threshold pressure $P_t$ as a function of the radial angle $\varphi$ for We $= 593$, $\alpha = 20°$ (solid blue line). The green, blue, and yellow areas illustrate pressure ranges for the normal splash, upward-only splash, and no splash, respectively. The thin dotted lines identify splash angles $\varphi_{\text{spl},d}$ defining location of the end of the splash zone for $P_t = 41, 43\,\text{kPa}$. (c) Variations of the threshold pressure $P_t$ as a function of the radial angle $\varphi$ for We $= 593$, $\alpha = 30°$ (solid orange line). The green, orange, and yellow areas illustrate pressure ranges for the normal splash, wing splash, and no splash, respectively. The thin dotted lines identify splash angles $\varphi_{\text{spl},d}$ defining location of the end of the splash zone for $P_t = 41, 43\,\text{kPa}$. (d) Variations of the threshold pressure $P_t$ as a function of the radial angle $\varphi$ for We $= 593$, $\alpha = 40°°$ (solid green line). The green and yellow areas illustrate pressure ranges for the normal splash and no splash conditions, respectively.

to abnormal splashing documented here. The theoretical model shows that normal splashing occurs for $P > 42.8\,\text{kPa}$, the wing splashing occurs for $36 < P < 42.8\,\text{kPa}$ and no splashing occurs for $P < 36\,\text{kPa}$. Now consider a certain value of the ambient pressure, e.g., $P = 39\,\text{kPa}$. Results given in Fig. 11(c) show that when $\varphi <\sim 70°$ or $\varphi >\sim 140°$ $P_t$'s are larger than this pressure and, therefore, no splashing can take place. Images displayed in Fig. 6(c) show splashing occurring for $71° \leqslant \varphi \leqslant 127°$ in reasonable agreement with these predictions. The reader should note that $P = 33\,\text{kPa}$ was used in the experiment and no splashing should take place under such conditions according to the theory. The error is associated with the error in measuring the threshold pressure for the orthogonal impact as discussed before, so only qualitative agreement between predictions and experiments can be claimed in this case.

It is shown that the nonmonotonic variations of the threshold pressure as a function of We can be directly observed in the splash evolution during an oblique impact. Both the upward-only

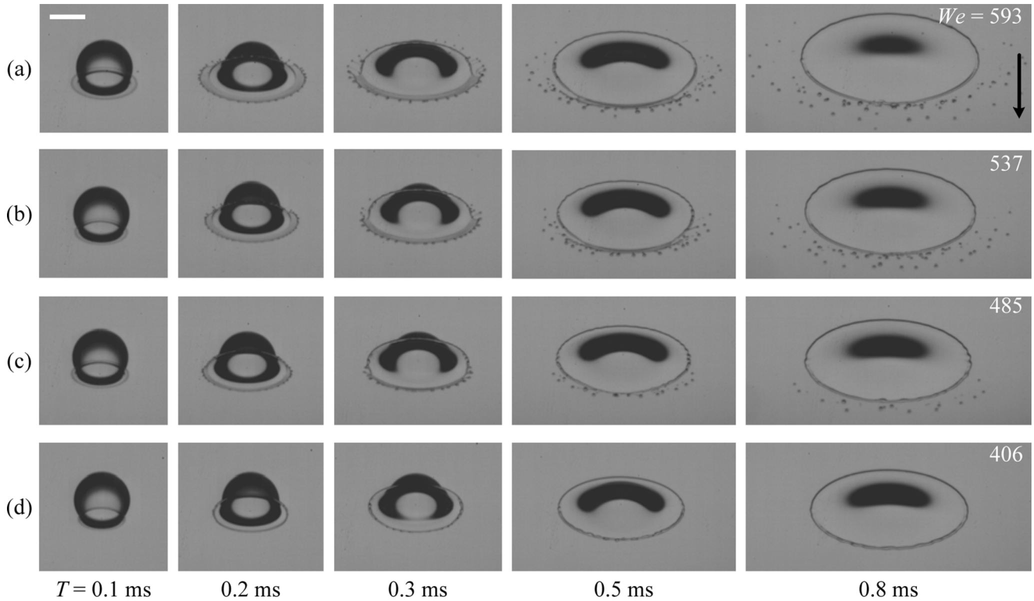


FIG. 12. Effect of the Weber number on the droplet splashing for $P = 51$ kPa, $\alpha = 30^{\circ}$ (see Movie S7 for more details [51]). Each column represents a different dimensional time $T$ and each row represents a different Weber number We. (a) We $= 593$, $\varphi_{\mathrm{spl}} = 30^{\circ}$. (b) We $= 537$, $\varphi_{\mathrm{spl}} = 68^{\circ}$. (c) We $= 485$, $\varphi_{\mathrm{spl}} = 124^{\circ}$. (d) We $= 406$, $\varphi_{\mathrm{spl}} = 180^{\circ}$.

splashing displayed in Figs. 6(c) and 6(d) and the wing splashing displayed in Fig. 7(c) contradict the assumption that it is the lift force (which is proportional to the lamella tip velocity) that drives the droplet splashing (see Sec. III and [17–19,38]) but phenomena illustrated in Figs. 3 and 4 support this assumption. The resolution of these differences and explanation of the processes dominating system response in each case deserve future scrutiny.

Figure 11(d) illustrates transition between the normal splash and no splash for We $= 593$, $\alpha = 40^{\circ}$. Normal splash occurs for $P > 36$ kPa and no splash for $P < 36$ kPa, in agreement with images displayed in Fig. 8.

### B. The fixed ambient pressure case

Results displayed in Fig. 12 show that the splash angle $\varphi_{\mathrm{spl}}$ increases monotonically with a decrease of We for $\alpha = 30^{\circ}$ for the constant ambient pressure of $P = 51$ kPa, while results displayed in Fig. 13 show that $\varphi_{\mathrm{spl}}$ increases monotonically with an increase of the inclination angle $\alpha$ for We $= 593$ and the same ambient pressure.

Variations of $\varphi_{\mathrm{spl}}$ as a function of We and $\alpha$ at $P = 51$ kPa illustrated in Fig. 14(a) demonstrate that $\varphi_{\mathrm{spl}}$ decreases monotonically with an increase in $\alpha$ and a decrease of We. Phenomenological results demonstrating similar dependencies are given in Figs. 12 and 13.

A similar process was used to determine $\varphi_{\mathrm{spl}}$ for various We's at $P = 51$ kPa. We determine the local EOWN as a function of the radial angle $\varphi$ and the Weber number We for $\alpha = 20^{\circ}$, with results illustrated using color lines in Fig. 14(b) and providing the basis for the determination of the threshold pressure $P_t$. The information flow required to determine $P_t$ is illustrated using orange dash-dotted lines, and the results of this process, i.e., computed $P_t$'s, are displayed in Fig. 14(c). To illustrate use of this figure, consider ambient pressure $P = 51$ kPa which is marked using a black dotted line. If $P_t$ at a given $\varphi$ and We is higher than 51 kPa, the lamella does not splash at this location at this We and at this pressure. Otherwise, splashing occurs. Intersection of line $P_t(\varphi)$ with the line

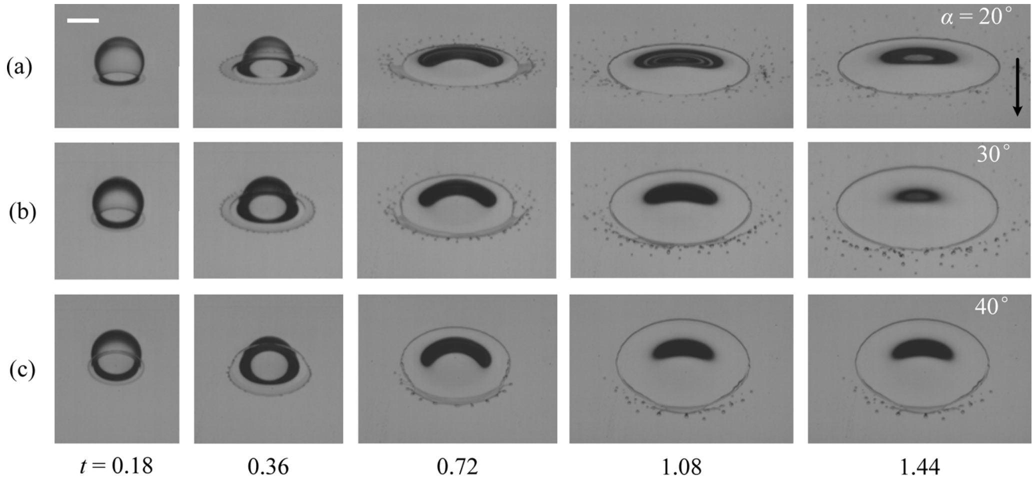


FIG. 13. Effect of the inclination angle $\alpha$ on the droplet splashing for $P = 51$ kPa, We = 593 (see Movie S8 for more details [51]). Each column represents a different dimensionless time $t$ and each row represents a different inclination angle. (a) $\alpha = 20°$, $\varphi_{spl} = 0°$. (b) $\alpha = 30°$, $\varphi_{spl} = 30°$. (c) $\alpha = 40°°$, $\varphi_{spl} = 108°$.

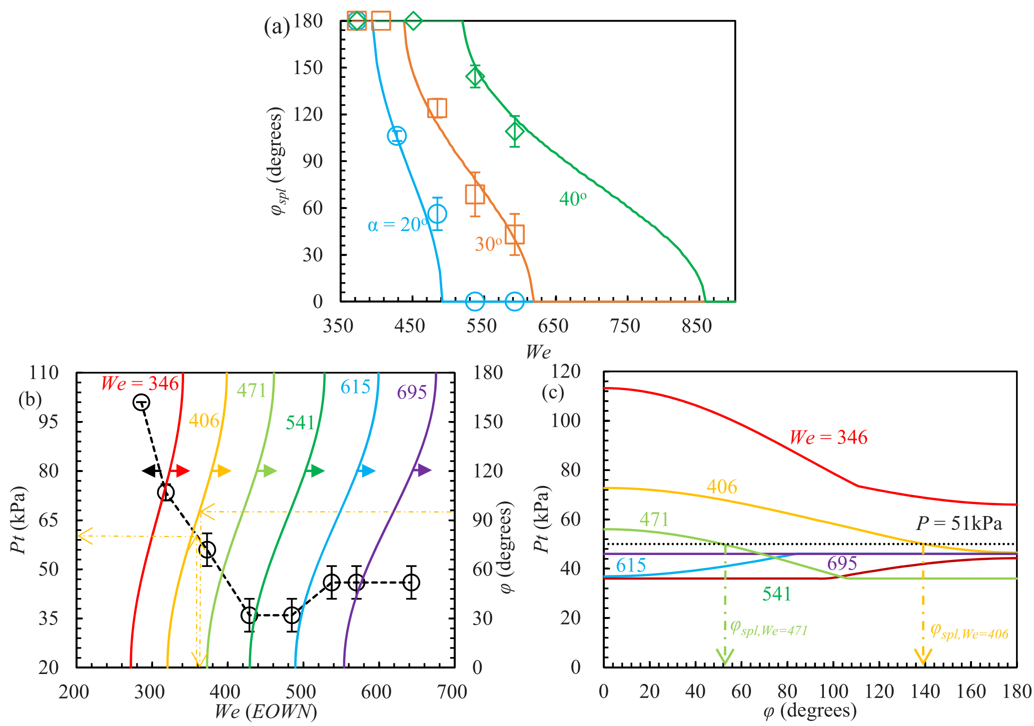


FIG. 14. (a) Variations of $\varphi_{spl}$ as a function of We for $P = 51$ kPa. Error bars indicate the standard deviation. The solid lines illustrate theoretical results. (b) Variations of the equivalent orthogonal Weber number (EOWN) as a function of the radial angle $\varphi$ for $\alpha = 20°$ for selected Weber numbers identified using color solid lines. The orange dash-dotted lines illustrate the information flow required for the determining $P_t$'s for a typical combination of $\varphi$ and We. Circles identify the experimentally determined $P_t$'s for the orthogonal impact. (c) Variations of the theoretically determined threshold pressure $P_t$ as a function of the radial angle $\varphi$ at various We's for $\alpha = 20°$. The dash-dotted lines illustrate information flow required for the determination of $\varphi_{spl,We}$ for selected We's for the ambient pressure of $P = 51$ kPa.

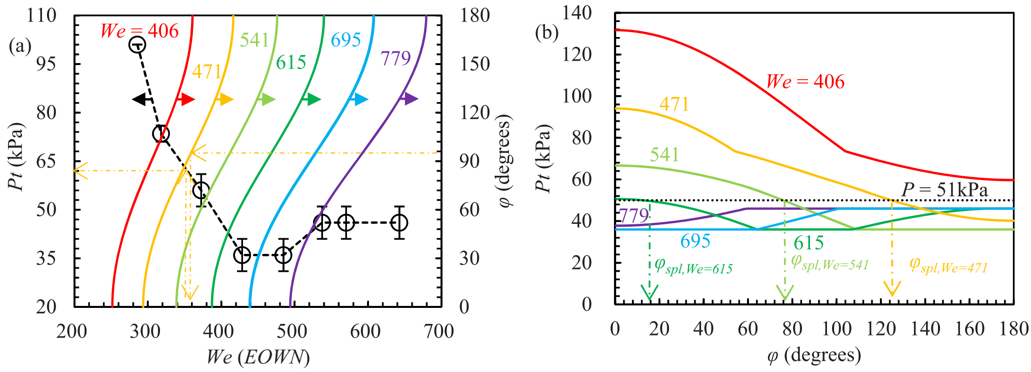


FIG. 15. (a) Variations of the equivalent orthogonal Weber number (EOWN) as a function of the radial angle $\varphi$ for $\alpha = 30^\circ$ for selected Weber numbers identified using color solid lines. The orange dash-dotted lines illustrate the information flow required for determination of $P_t$'s for a typical combination of $\varphi$ and We. Circles identify the experimentally determined $P_t$'s for the orthogonal impact. (b) Variations of the theoretically determined threshold pressure $P_t$ as a function of the radial angle $\varphi$ at various We's for $\alpha = 30^\circ$. The dash-dotted lines illustrate information flow required for the determination of $\varphi_{\mathrm{spl,We}}$ for selected We's for the ambient pressure of $P = 51$ kPa.

giving the ambient pressure $P = 51$ kPa defines the threshold angle $\varphi_{\mathrm{spl,We}}$ for this Weber number at $P = 51$ kPa with splashing occurring for $\varphi > \varphi_{\mathrm{spl,We}}$. These thresholds are marked in Fig. 14(c) for We = 406, 471 as $\varphi_{\mathrm{spl,We=406}}$ and $\varphi_{\mathrm{spl,We=471}}$, respectively. The theoretically determined $\varphi_{\mathrm{spl}}$'s are illustrated using blue line in Fig. 14(a) and are consistent with the experimental data points given by blue circles in Fig. 14(a). The reader may note that these predictions are affected by the error in the determination of the threshold pressure for the orthogonal impact.

Similar analysis is repeated for $\alpha = 30^\circ$, with results displayed in Figs. 15(a) and 15(b). The theoretically determined $\varphi_{\mathrm{spl}}$'s are illustrated using orange line in Fig. 14(a) and are consistent with the experimental observations [see orange rectangles in Fig. 14(a)].

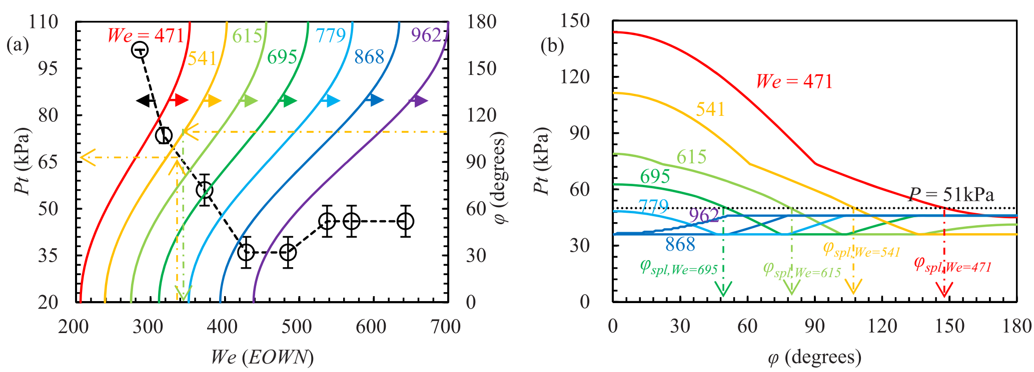


FIG. 16. (a) Variations of the equivalent orthogonal Weber number (EOWN) as a function of the radial angle $\varphi$ for $\alpha = 40^\circ$ for selected Weber numbers identified using color solid lines. The orange dash-dotted lines illustrate the information flow required for determination of $P_t$'s for a typical combination of $\varphi$ and We. Circles identify the experimentally determined $P_t$'s for the orthogonal impact. (b) Variations of the theoretically determined threshold pressure $P_t$ as a function of the radial angle $\varphi$ at various We's for $\alpha = 40^\circ$. The dash-dotted lines with arrows illustrate information flow for determination of $\varphi_{\mathrm{spl,We}}$ for selected We's for the ambient pressure of $P = 51$ kPa.

The same analysis has been carried out for $\alpha = 40^\circ$ with results displayed in Figs. 16(a) and 16(b). The theoretically determined $\varphi_{spl}$'s are illustrated using the green line in Fig. 14(a) and are consistent with the experimental observations [see green diamonds in Fig. 14(a)].

## V. CONCLUSION

Droplet impacts on inclined surfaces were observed from underneath the impacted plate using the droplet as a lens. It was found that the lamella maintained a circular shape during the early stages of the impact. The splash angle $\varphi_{spl}$ increased monotonically with an increase of the Weber number We and a decrease of the inclination angle $\alpha$ at atmospheric pressure, whereas abnormal splashing was observed at reduced pressures. Predictions based on an extended model match the experiments and suggest that the outward velocity of the lamella tip determines the splash onset even for abnormal splashes. The abnormal splashing is shown to be a direct consequence of the nonmonotonic variations of the threshold pressure as a function of the Weber number for orthogonal impacts. The results provide a basis for the development of splash control strategies based on the combination of the inclination angle and the ambient pressure, including control of the location and size of the splashing zone.

## ACKNOWLEDGMENTS

We would like to thank Prof. S. Ma, Prof. Q. Tian, and Dr. Q. Ma, for kindly providing us the high-speed camera. This study was financially supported by National Key R&D Program of China under Grant No. 2018YFF0300800, the National Natural Science Foundation of China under Grant No. 51406012, and 111 Project under Grant No. B16003.

---

[1] C. Josserand and S. T. Thoroddsen, Drop impact on a solid surface, Annu. Rev. Fluid Mech. **48**, 365 (2016).

[2] A. L. Yarin, Drop impact dynamics: splashing, spreading, receding, bouncing …, Annu. Rev. Fluid Mech. **38**, 159 (2006).

[3] S. T. Thoroddsen, T. G. Etoh, and K. Takehara, High-speed imaging of drops and bubbles, Annu. Rev. Fluid Mech. **40**, 257 (2008).

[4] G. Liang and I. Mudawar, Review of drop impact on heated walls, Int. J. Heat Mass Tran. **106**, 103 (2017).

[5] A. M. Worthington, On the forms assumed by drops of fluids falling vertically on a horizontal plate, Proc. R. Soc. London **25**, 261 (1876).

[6] C. D. Stow and M. G. Hadfield, An experimental investigation of fluid flow resulting from the impact of a water drop with an unyielding dry surface, Proc. R. Soc. A. **373**, 419 (1981).

[7] C. Mundo, M. Sommerfeld, and C. Tropea, Droplet-wall collisions: experimental studies of the deformation and breakup process, Int. J. Multiphase Flow **21**, 151 (1995).

[8] S. T. Thoroddsen, K. Takehara, and T. G. Etoh, Micro-splashing by drop impacts, J. Fluid Mech. **706**, 560 (2012).

[9] L. Xu, Liquid drop splashing on smooth, rough, and textured surfaces, Phys. Rev. E. **75**, 056316 (2007).

[10] J. Liu, H. Vu, S. S. Yoon, R. Jepsen, and G. Aguilar, Splashing phenomena during liquid droplet impact, Atom. Spray. **20**, 297 (2010).

[11] Y. Liu, P. Tan, and L. Xu, Kelvin–Helmholtz instability in an ultrathin air film causes drop splashing on smooth surfaces, Proc. Natl. Acad. Sci. USA **112**, 3280 (2015).

[12] Z. Jian, C. Josserand, S. Popinet, P. Ray, and S. Zaleski, Two mechanisms of droplet splashing on a solid substrate, J. Fluid Mech. **835**, 1065 (2018).

[13] S. Mandre, M. Mani, and M. P. Brenner, Precursors to Splashing of Liquid Droplets on a Solid Surface, Phys. Rev. Lett. **102**, 134502 (2009).

[14] S. Mandre and M. P. Brenner, The mechanism of a splash on a dry solid surface, J. Fluid Mech. **690**, 148 (2012).
[15] J. M. Kolinski, S. M. Rubinstein, S. Mandre, M. P. Brenner, D. A. Weitz, and L. Mahadevan, Skating on a Film of Air: Drops Impacting on a Surface, Phys. Rev. Lett. **108**, 074503 (2012).
[16] L. Duchemin and C. Josserand, Rarefied gas correction for the bubble entrapment singularity in drop impacts, C. R. Mec. **340**, 797 (2012).
[17] G. Riboux and J. M. Gordillo, Experiments of Drops Impacting a Smooth Solid Surface: A Model of the Critical Impact Speed for Drop Splashing, Phys. Rev. Lett. **113**, 024507 (2014).
[18] G. Riboux and J. M. Gordillo, Boundary-layer effects in droplet splashing, Phys. Rev. E. **96**, 013105 (2017).
[19] J. M. Gordillo and G. Riboux, A note on the aerodynamic splashing of droplets, J. Fluid Mech. **871**, R3 (2019).
[20] R. Rioboo, C. Tropea, and M. Marengo, Outcomes from a drop impact on solid surfaces, Atom. Spray. **11**, 155 (2001).
[21] J. Palacios, J. Hernandez, P. Gomez, C. Zanzi, and J. Lopez, Experimental study of splashing patterns and the splashing/deposition threshold in drop impacts onto dry smooth solid surfaces, Exp. Therm. Fluid Sci. **44**, 571 (2013).
[22] J. Hao, Effect of surface roughness on droplet splashing, Phys. Fluids **29**, 122105 (2017).
[23] C. S. Stevens, A. Latka, and S. R. Nagel, Comparison of splashing in high- and low-viscosity liquids, Phys. Rev. E. **89**, 063006 (2014).
[24] T. C. de Goede, N. Laan, K. G. de Bruin, and D. Bonn, Effect of wetting on drop splashing of newtonian fluids and blood, Langmuir **34**, 5163 (2018).
[25] E. S. Quintero, G. Riboux, and J. M. Gordillo, Splashing of droplets impacting superhydrophobic substrates, J. Fluid Mech. **870**, 175 (2019).
[26] M. A. Quetzeri-Santiago, K. Yokoi, A. A. Castrejón-Pita, and J. R. Castrejón-Pita, The Role of the Dynamic Contact Angle on Splashing, Phys. Rev. Lett. **122**, 228001 (2019).
[27] K. Range and F. Feuillebois, Influence of surface roughness on liquid drop impact, J Colloid Interface Sci. **203**, 16 (1998).
[28] L. Xu, L. Barcos, and S. R. Nagel, Splashing of liquids: Interplay of surface roughness with surrounding gas, Phys. Rev. E. **76**, 066311 (2007).
[29] A. Latka, A. Strandburg-Peshkin, M. M. Driscoll, C. S. Stevens, and S. R. Nagel, Creation of Prompt and Thin-Sheet Splashing by Varying Surface Roughness or Increasing Air Pressure, Phys. Rev. Lett. **109**, 054501 (2012).
[30] I. Roisman, A. Lembach, and C. Tropea, Drop splashing induced by target roughness and porosity: the size plays no role, Adv. Colloid Interfac. **222**, 615 (2015).
[31] J. C. Bird, S. Tsai, and H. A. Stone, Inclined to splash: triggering and inhibiting a splash with tangential velocity, New J. Phys. **11**, 063017 (2009).
[32] J. Hao and S. I. Green, Splash threshold of a droplet impacting a moving substrate, Phys. Fluids **29**, 012103 (2017).
[33] H. Almohammadi and A. Amirfazli, Understanding the drop impact on moving hydrophilic and hydrophobic surfaces, Soft Matter **13**, 2040 (2017).
[34] K. A. Raman, Normal and oblique droplet impingement dynamics on moving dry walls, Phys. Rev. E. **99**, 053108 (2019).
[35] Š. Šikalo, C. Tropea, and E. N. Ganic, Impact of droplets onto inclined surfaces, J. Colloid Interf. Sci. **286**, 661 (2005).
[36] L. Courbin, J. C. Bird, and H. A. Stone, Splash and anti-splash: observation and design, Chaos **16**, 041102 (2006).
[37] D. G. K. Aboud and A. M. Kietzig, Splashing threshold of oblique droplet impacts on surfaces of various wettability, Langmuir **31**, 10100 (2015).
[38] J. Hao, J. Lu, L. Lee, Z. Wu, G. Hu, and J. M. Floryan, Droplet Splashing on an Inclined Surface, Phys. Rev. Lett. **122**, 054501 (2019).

[39] H. J. J. Staat, T. Tran, B. Geerdink, G. Riboux, C. Sun, J. M. Gordillo, and D. Lohse, Phase diagram for droplet impact on superheated surfaces, J. Fluid Mech. **779**, R3 (2015).
[40] G. Riboux and J. M. Gordillo, Maximum drop radius and critical Weber number for splashing in the dynamical Leidenfrost regime, J. Fluid Mech. **803**, 516 (2016).
[41] C. J. Howland, A. Antkowiak, J. R. Castrejón-Pita, S. D. Howison, J. M. Oliver, R. W. Style, and A. A. Castrejón-Pita, It's Harder to Splash on Soft Solids, Phys. Rev. Lett. **117**, 184502 (2016).
[42] L. Xu, W. W. Zhang, and S. R. Nagel, Drop Splashing on a Dry Smooth Surface, Phys. Rev. Lett. **94**, 184505 (2005).
[43] M. M. Driscoll and S. R. Nagel, Ultrafast Interference Imaging of Air in Splashing Dynamics, Phys. Rev. Lett. **107**, 154502 (2011).
[44] R. C. A. van der Veen, T. Tran, D. Lohse, and C. Sun, Direct measurements of air layer profiles under impacting droplets using high-speed color interferometry, Phys. Rev. E **85**, 026315 (2012).
[45] Y. Liu, P. Tan, and L. Xu, Compressible air entrapment in high-speed drop impacts on solid surfaces, J. Fluid Mech. **716**, R9 (2013).
[46] J. de Ruiter, R. Lagraauw, D. van den Ende, and F. Mugele, Wettability-independent bouncing on flat surfaces mediated by thin air films, Nat. Phys. **11**, 48 (2015).
[47] E. Q. Li and S. T. Thoroddsen, Time-resolved imaging of a compressible air disc under a drop impacting on a solid surface, J. Fluid Mech. **780**, 636 (2015).
[48] H. Y. Lo, Y. Liu, and L. Xu, Mechanism of Contact Between a Droplet and an Atomically Smooth Substrate, Phys. Rev. X **7**, 021036 (2017).
[49] E. Q. Li, K. R. Langley, Y. S. Tian, P. D. Hicks, and S. T. Thoroddsen, Double Contact During Drop Impact on a Solid Under Reduced Air Pressure, Phys. Rev. Lett. **119**, 214502 (2017).
[50] M. J. Thoraval, K. Takehara, T. G. Etoh, and S. T. Thoroddsen, Drop impact entrapment of bubble rings, J. Fluid Mech. **724**, 234 (2016).
[51] See Supplemental Material at http://link.aps.org/supplemental/10.1103/PhysRevFluids.5.073603 for supplementary movies with commentaries.